

An Integrated Mathematical Model for Ironmaking Blast Furnace



LINGLING LIU, BAOYU GUO, SHIBO KUANG, and AIBING YU

This paper presents an integrated model by combining the raceway combustion model, the process model, and the hearth flow and heat transfer model for simulating an entire ironmaking blast furnace (BF). This integration eliminates major assumptions at the boundaries shared by these sub-models and enables linking the model with operating parameters at the BF top and bottom directly. The applicability of this integration is first examined through various applications. On this base, the usefulness of the integrated model is demonstrated by studying the effect of burden distribution on the in-furnace states of a 5000 m³ industrial BF. The simulation results with and without the integration are compared. Also, *via* the integrated model, the effect of the ore-to-coke (O/C) radial profile at the burden surface is evaluated in terms of internal flow and thermochemical behaviors as well as overall process performance. It is shown that for given BF conditions except for the O/C radial profile, the indirect reduction in the upper furnace increases with the improvement of uniformity in the radial profile, leading to higher top gas utilization and lower productivity. Meanwhile, the hearth center tends to develop lower temperatures and stronger natural convection that reduces the heat loss through hearth walls. This integrated model would open up a cost-effective method to examine the effect of top and bottom factors on BF performance under different conditions in a comprehensive matter.

<https://doi.org/10.1007/s11663-020-01905-w>

© The Minerals, Metals & Materials Society and ASM International 2020

I. INTRODUCTION

BLAST furnace (BF) ironmaking is the most important technology by which pig iron is reduced from ferrous materials. As an energy-intensive process, the BF ironmaking process, together with the associated units (*e.g.*, pelletizing–sintering machine and coke oven), represent approximately 70 pct of the total energy input into an integrated steelwork and contributes approximately 90 pct of the total CO₂ emission. Therefore, it is necessary to optimize the BF ironmaking process for minimizing fuel consumption and mitigating CO₂ emission, which becomes particularly important under increasingly demanding and tough economic and environmental conditions. To achieve this goal, the heat exchange and chemical reactions between different

phases need to be effectively controlled in every region or zone of a BF. In this direction, understanding the in-furnace states and the resulting overall performance of BF under different conditions is important.

BF is a high-temperature and high-pressure moving bed reactor, in which the counter-, co-, and cross-current flows of gas, liquid, solid, and powder interact strongly, coupled with the heat and mass transfer and chemical reactions. In routine operations, the burden materials that consist of iron-bearing ore and coke with flux are alternately charged into the top of a BF. Meanwhile, the oxygen-rich hot air and pulverized coal (PC) are injected into the BF through tuyeres near the bottom, forming a cavity known as the raceway. In the raceway region, PC and coke combust with hot air, generating reducing gases and smelting heat. During the burden descent, the ore is reduced and heated by the ascending gas before it melts in the cohesive zone (CZ) forming liquid slag and iron. The liquids then percolate through the coke bed to the hearth and are periodically drained out through a taphole. The coke bed in the hearth may float in the hot metal (*viz.* floating coke bed), rest on the refractory pad near the middle of the hearth (*viz.* sitting coke bed with coke free gutter), or fill the hearth completely (*viz.* sitting coke bed), leading to different liquid flow behaviors.

LINGLING LIU, BAOYU GUO, and SHIBO KUANG are with the ARC Research Hub for Computational Particle Technology, Department of Chemical Engineering, Monash University, Clayton, VIC 3800, Australia. Contact e-mail: shibo.kuang@monash.edu
AIBING YU are with the ARC Research Hub for Computational Particle Technology, Department of Chemical Engineering, Monash University and Center for Simulation and Modeling of Particulate Systems, Southeast University-Monash University Joint Research Institute, Suzhou Industrial park, Jiangsu 215213, P.R. China. Contact e-mail: aibing.yu@monash.edu.

Manuscript submitted March 31, 2020.

Article published online July 13, 2020.

Because of the complexity of BF, it has been a challenge to access the above in-furnace phenomena by means of physical experiments and/or in-suite measurements. Numerical models can in principle overcome this problem and have the merits of high efficiency and low cost while providing some direct mechanistic insights. Therefore, such an approach has been widely used to study the BF ironmaking process in recent years, as reviewed by different investigators.^[1–6] Because transport phenomena inside a BF occur at different length and time scales, it is extremely difficult to describe the entire BF process by a single method. For this reason, the whole BF can be divided into four main regions including the burden charging system, the raceway, the main body, and the hearth, and these regions can be modeled separately using different methods.^[1] The latter three regions that deal with iron ore reduction and melting as well as liquid drainage are focused in this study. The relevant modeling efforts are briefly reviewed below.

The modeling of the raceway region has focused mainly on cavity formation^[7,8] and combustion.^[9,10] This is often done separately by considering either the lower part of a BF or a box-shaped packed bed containing one tuyere. In a raceway model, the blast and PCI conditions as simulation inputs are directly linked with practical operational parameters. This is often not the case for a hearth model that only considers the region below the slag surface. Generally, hearth models have different focuses, including the transient drainage process,^[11,12] the line erosion,^[13,14] as well as localized flow and heat transfer behaviors.^[15–17]

Different from hearth and raceway models that focus on local phenomena, a process model that simulates the region between burden and slag surfaces can predict the overall performance of a BF and the associated in-furnace states to a large degree. Toward this target, many efforts have been made in the past to describe the primary phenomena related to gas, solid, liquid, and powder phases inside the main body region based on discrete- and continuum-based models. Some examples include the modeling of solid flow and deadman,^[18–21] heat transfer and chemical reactions,^[22–24] liquid flow in the form of droplet/rivulet,^[25–29] transient behaviors,^[30,31] layered burden and CZ,^[32–37] powder flow,^[22,38,39] and stockline variation.^[35] Different combinations of these developments have led to different BF process models.^[22,30,32–34,36,37,39–46]

To better evaluate BF performance, the process model, the raceway model, and the hearth model should be used together. However, these sub-models have often been used individually, with certain assumptions made at the shared interfaces. For example, the raceway and the hearth regions are simplified as the input and output boundaries in a process model. Therein, the reducing gas conditions in the raceway as the inlet conditions are determined according to the statistic results of a raceway combustion model,^[34, 36,47] or the local mass and energy conservation with a pre-set coal burnout.^[22,32,33,35,37,44] Meanwhile, the computational domain of the process

model covers the region only from the burden surface to the slag surface, hence the taphole liquid temperature cannot be predicted directly.^[22,32,33,35,37,44,47,48] In a hearth model, the mass and velocity distributions of liquid iron and slag entering the hearth are sometimes empirically specified with a “peripheral pattern” or a “uniform pattern”.^[49,50]

In the past, a few efforts have been made to overcome the above problems. For example, the modeling of raceway cavity^[47] and even the coke/coal combustions in the raceway region^[39,43] have been incorporated into a process model. However, in those works, some other main features in the raceway region remain unsolved, including, for instance, the widely recognized recirculating vortex and its influence on the reducing gas redistribution and the coal burnout efficiency. Consequently, how this recirculating vortex and the resulting anisotropic combustion behavior affect the in-furnace states and overall BF performance is unclear. Recently, Fu *et al.*^[51] integrated a raceway model into a process model but focused on the evaluation of the effects of pulverized coal injection (PCI) conditions on coal burnout and BF overall performance. Inada *et al.*^[52] interlinked their in-house 3D dynamic process model^[44] and hearth erosion model^[53] with each other. To our knowledge, a model of integrating the hearth model, the raceway model and the process model for simulating an entire BF has not been reported in the literature.

In this article, to overcome this problem, we have developed a numerical model by integrating our ANSYS CFX-based raceway combustion model,^[54] process model,^[47] and hearth flow and heat transfer model.^[50] This integration aims to link together our major BF modeling efforts in recent years, and to eliminate the major assumptions at the interfaces between these sub-models, so as to generate a more comprehensive picture about BF. The structure of this article is as follows. First, the model development is outlined. Then, the applicability of the sub-models and the integrated model is examined through various applications. On this base, a 5000 m³ industrial BF is simulated with or without the integration, and the results are compared. Finally, the in-furnace states inside the main body, hearth, and raceway regions and the BF overall performance are studied with respect to different burden distributions to demonstrate the usefulness of the integrated model.

II. MODEL DESCRIPTION

A. Integrating Strategy

The current model considers a BF from the burden surface at the top to the hearth at the bottom. It integrates the previously developed ANSYS CFX-based sub-models such as the raceway combustion model,^[54] the process model,^[47] and the hearth flow and heat transfer model^[49] through shared libraries and user-defined functions.

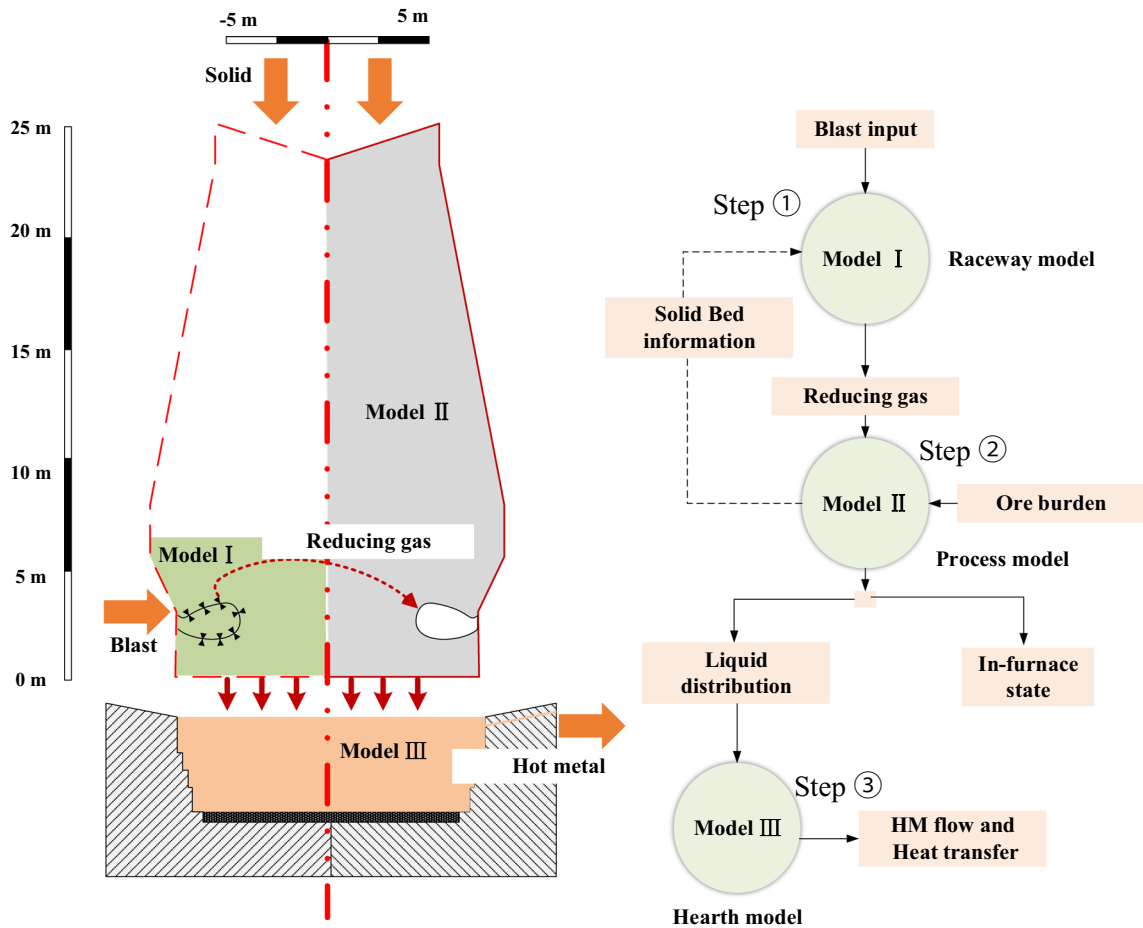


Fig. 1—Strategy of integrating raceway, process, and hearth models.

Figure 1 illustrates how the three sub-models are integrated. First, the coal combustion and associated flow, heat and mass transfer in the blowpipe, tuyere, and raceway are simulated using the raceway combustion model (model I) under the given blast conditions and coal injection rate. Then, the resulting reducing gas velocity, temperature, component fractions, and mass flow rate on the outer surface of the raceway cavity are extracted and passed on to the process model (model II) *via* a shared library. In this process, the coke bed overlapping with the region in the raceway model is omitted. Also, the raceway outer surface is treated as the inlet boundary of the process model that excludes the raceway cavity considered in the raceway model. With the reducing conditions at the raceway surface as well as the given solid conditions at the burden surface, the in-furnace states and overall performance parameters are calculated using the process model; it generates the distributions of liquid temperature and velocities at the slag surface. Again, *via* a shared library, these liquid distributions are mapped from the process model to the inlet boundary of the hearth flow and heat transfer model (model III). Finally, the temperature profile and flow regimes inside the hearth are obtained using the hearth model.

B. Governing Equations

Table I lists the governing equations of the integrated model, which corresponds to the raceway model, process model, and hearth model. These sub-models and their numerical treatments have been detailed elsewhere.^[10,21,32,35,45,47,49,50,54,55] Below, only the key features of each sub-model are outlined for brevity. In the raceway combustion model,^[54] the pulverized coal is regarded as a discrete phase and tracked by the Lagrangian Particle Tracking (LPT) method, while the blast is treated with the continuum method and solved by Computational Fluid Dynamics (CFD). The porous media module is adopted, and the Ergun equation is applied to account for the bed pressure loss. The heat, mass, and momentum transfer between gas and solid phases and between gas and pulverized coal are considered. Besides, the thermal radiation is included for better determining the thermal behaviors at high temperatures.

In the process model,^[47] the moving bed is modeled using a porous media module, in which the gas, solid and liquid phases are treated as interpenetrating continua. The interphase heat, mass, and momentum transfer between gas, liquid, and solid are enabled. The pressure loss in the gas phase is determined with the Ergun equation, where the bed permeability is jointly

Table I. Governing Equations of the Present Model

Process Model	
mass balance	$\nabla \cdot (\varepsilon_i \rho_i U_i) = S_i$
gas momentum	$\nabla \cdot (\varepsilon_g \rho_g U_g U_g) = \nabla \cdot \tau_g - \varepsilon_g \nabla p + \rho_g \varepsilon_g \mathbf{g} + f_g^s + f_g^{l,d}$
solid momentum	$\nabla \cdot (\varepsilon_s \rho_s U_s U_s) = \nabla \cdot \tau_s - \varepsilon_s \nabla p_s + \rho_s \varepsilon_s \mathbf{g}$
liquid momentum	$f_{l,d}^s + f_{l,d}^s + \varepsilon_l \rho_l \mathbf{g} = 0$
heat and species	$\nabla (\varepsilon_i \rho_i U_i \theta_{i,m}) - \nabla (\varepsilon_i \Gamma_i \nabla \theta_{i,m}) = S_{\theta_{i,m}}$
volume fraction	$\varepsilon_s + \varepsilon_g + \varepsilon_l = 1$
Raceway Model	
mass balance	$\nabla \cdot (\varepsilon \rho U) = S$
gas momentum	$\nabla \cdot (\varepsilon_g U_g U_g) = \nabla \cdot \tau_g - \varepsilon_g \nabla p + \rho_g \varepsilon_g \mathbf{g} + f_g^s$
heat and species	$\nabla (\varepsilon \rho U \theta) - \nabla (\varepsilon \Gamma \nabla \theta) = S_\theta$
particle motion	$\frac{dm_p}{dt} = -\dot{m}, m_p \frac{dU_p}{dt} = -f_D, f_D = -\frac{1}{8} \pi d_p^2 \rho C_D U_g - U_p (U_g - U_p)$
particle energy	$m_p C_p \frac{dT_p}{dt} = -\pi d_p \lambda Nu (T_g - T_p) + \sum \frac{dm_p}{dt} H_{\text{reac}} + A_p \varepsilon_p (\pi I - \sigma_B T_p^4)$
Hearth Model	
mass balance	$\nabla \cdot (\varepsilon \rho_l U_l) = 0$
momentum	$\nabla \cdot (\varepsilon \rho_l U_l U_l) = \nabla \cdot \tau_l - \varepsilon \nabla p - g \rho_l \beta (T_l - T_{ref}) - \varepsilon R$
energy	$\varepsilon \rho_l C_l \nabla \cdot (U_l T_l) - \nabla \cdot (\lambda \cdot \nabla T) = 0$

determined by the burden distribution and thermal state of ores (shrinkage ratio). The streamlines of solid phase are created first, along which the structural properties (e.g., voidage, size) can be convected downwards during the descent of solids. Shrinkage ratio Sh is introduced to model the ore melting process.^[32] The cohesive zone is presumed to lie between 1200 °C and 1400 °C of the solid temperature, corresponding to the value of Sh from 0 to 1. The shape and position of the deadman are predicted by a viscous flow model. The coke size and the porosity in deadman are, respectively, set to 0.35 and 0.02 m according to the normal BF practice.^[38] The liquid phase is treated as a mixture that consists of hot metal and slag.

In the hearth model, a single-phase flow through a porous medium with conjugate heat transfer between liquid and refractories is considered. The drainage process is assumed to be continuous and simulated by the model that considers the buoyancy force,^[50] and the thermal dispersion term and the modification of the turbulence model.^[49] Although various coke bed shapes and positions may be observed in the hearth,^[1,2] a “fully sitting bed” with a bed porosity of 0.35 and a particle size of 0.02 m is considered in this study. Under such a condition, the coke bed extends from the deadman to the hearth bottom. Considering that the deadman may affect BF performance substantially, it would be useful to develop a numerical model to predict the state of the coke bed and its particle size and porosity distributions under different conditions. Discrete element modeling should be useful and preferred in this respect.^[1] Additionally,

in the current hearth model, coke and iron temperatures are assumed equal. Two lining materials are considered: the inner ceramic cup and the outer fire brick.^[50] The taphole is represented by a hollow enclosure without coke inside it.

C. Chemical Reactions

Table II summarizes the major chemical reactions that are explicitly considered in this work. The combustion behaviors in the raceway region are described in terms of the coke combustion and carbon solution for the coke bed, as well as the coal devolatilization, volatile matter combustion, char combustion, and “char solution” for the coal combustion. Here, the coal devolatilization and volatile matter combustion represent two devolatilization routes, namely, VM1 at a low temperature and VM2 at a high temperature. In the main body region, the reactions considered include the indirect and direct reduction of iron ore, melting, coke combustion, and carbon solution. Note that the modeling of coke combustion in the main body region is necessary for the process model as it may take place near the raceway surface with the remaining oxygen. Such a reaction is often ignored in the existing process models. This is the case for the current process model without integration. Additionally, the ore reduction is assumed to be completed within the CZ, as done previously.^[35,38]

Besides, some reactions are modeled implicitly. This is done by only considering their heat sinks and carbon assumptions to maintain global heat and mass balance. This is the case for the reduction of Si, the

Table II. Chemical Reactions Considered in the Present Study

Reactions	Reaction Formula	Reaction Rate Equation	Sub-models
Indirect Reduction	$\text{Fe}_2\text{O}_3 + 3\text{CO} \rightarrow 2\text{Fe} + 3\text{CO}_2$	$\frac{12k_{\text{ind}}^{\text{ore}} P(\text{CO})^3}{8.314T_s} \left/ \left\{ D_g \left[(1-f_0)^{-\frac{1}{3}} - 1 \right] + d_{\text{ore}} \left[k_1 \left(1 + \frac{1}{k_1} \right) \right]^{-1} \right\} \right.$	model II
Direct Reduction	$\text{FeO}_{(l)} + \text{C} \rightarrow \text{Fe}_{(l)} + \text{CO}$	$k_2 \frac{A}{r_b} \alpha_{\text{FeO}}$	model II
Carbon solution	$\text{CO}_2 + \text{C} \rightarrow 2\text{CO}$	$\frac{6k_{\text{c}}^{\text{coke}} P_{\text{CO}_2}}{8.314T_s} \left/ \left\{ \frac{d_{\text{coke}}}{k_f} + \frac{6}{\rho_{\text{coke}} E_f k_3} \right\} \right.$	models I & II
Coke Combustion	$2\text{C} + \text{O}_2 \rightarrow 2\text{CO}$	$\left(\frac{1}{k_d} + \frac{1}{k_c} \right)^{-1} [i] \pi d_c^2 \frac{P}{F_A}$	models I & II
Melting Reaction	$\text{FeO}_{(s)} \rightarrow \text{FeO}_{(l)}$	$\frac{T_l - T_{\text{min,sm}}}{T_{\text{max,sm}} - T_{\text{min,sm}}} \frac{0 \cdot \dot{m}_{\text{sm}} \rho_i \rho_i d_i A}{M_{\text{sm}} F_{\text{O,est}}} \left(\frac{T}{T_p} \right)$	model II
Coal Devolatilization	$\text{Coal}_{(s)} = \text{VM}_{(g)} + \text{Char}_{(s)}$	$\frac{dV_M}{dt} = (\alpha_1 k_1 + \alpha_2 k_2) C_0; k = A e^{\left(\frac{-E}{RT} \right)}$	model I
VM Combustion	$\text{VM}_{(g)} + \text{O}_2 \rightarrow \text{CO}_2 + \text{H}_2\text{O}$	$C_A \frac{f}{k} \min \left(\frac{[j]}{v_i} \right)$	model I
Char Combustion	$\text{Char} + \text{O}_2 \rightarrow \text{CO} + \text{CO}_2$	$\frac{d[m_c]}{dt} = - \frac{30}{1-e} \frac{M_c}{M_{\text{O}_2}} \frac{\rho_{\infty}}{\rho} \left(k_1 + (k_2 + k_3)^{-1} \right)^{-1} m_c$	model I
Char Solution	$\text{Char} + \text{CO}_2 \rightarrow 2\text{CO}$	$\frac{2(\theta-1)}{2-\theta} = A_s e^{\left(\frac{-E_s}{RT} \right)}$ $k_1 = \frac{2}{T_p}; D = \frac{D_{\text{ref}}}{\rho} \left(\frac{T_p + T_c}{2T_{\text{ref}}} \right)^{0.75}$	model I
		$k_2 = (1-e) \frac{k_c}{T_p}; k_3 = \frac{k_c T_p (\beta \coth \beta - 1)}{\beta^2 a};$ $k_c = A_c T_p e^{\left(\frac{-E_c}{RT} \right)}; \beta = R \left(\frac{k_c}{D_{\text{ref}}} \right)^{0.5}$	

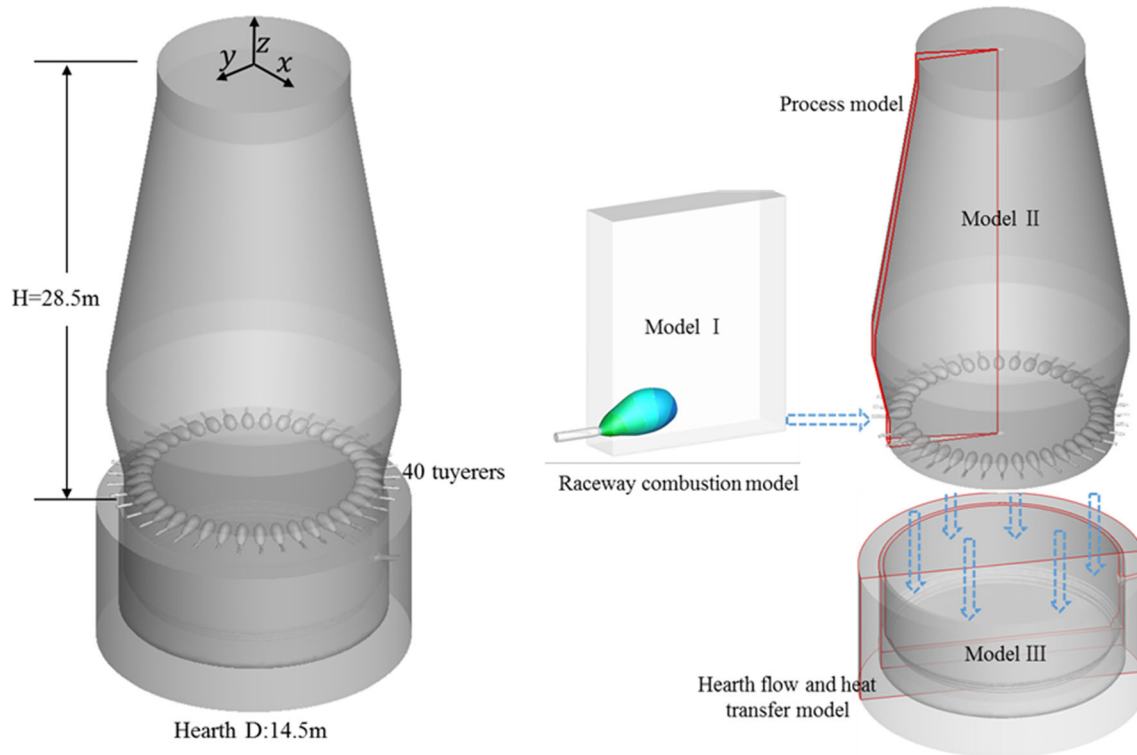


Fig. 2—Computational domain of the 5000 m³ industrial BF.

carburization reaction, and the melting of slag that consists of FeO and gangue materials. The reduction of S, P, Mn, or the like is neglected considering their small contents in hot metal, similar to the previous treatments.^[22,32–34,36,44,46,60] The carburization and silica reduction are modeled according to given carbon and silicon contents in the hot metal, which are 4 and 0.4 pct in mass. However, it should be pointed out that in the BF practice, both silicon and carbon contents in hot metal may vary with operating conditions and material properties. Thus, it would be useful to develop sub-models to predict silicon and carbon contents. This will be considered in our future work.

III. SIMULATION CONDITIONS

A. Computational Domain of Each Sub-model

Figure 2 shows the computational domains considered. To alleviate computational loadings, a rectangular packed bed with one tuyere is simulated by the raceway model. A pre-defined profile of the raceway cavity is assumed, of which the shape is given according to DEM simulations,^[10] and the dimensions (1.8 m in depth, 0.9 m in height) are determined according to the blast rate, pressure, temperature, and coke size in the deadman using Nomura's empirical correlations.^[56] The process model simulates a 9-deg sector of the BF containing a

raceway of one tuyere and treats the outer surface of the raceway as the gas inlet. Unless otherwise specified, the flow, mass, and temperature distributions of the reducing gas on this surface are provided by the raceway combustion model. The hearth geometry is assumed to be plane-symmetric and a 180-deg 3D structure is simulated. The liquid temperature and velocity profiles at the inlet are set by expanding those obtained using the process model.

B. Operational Conditions

Table III lists the simulation conditions used in the current study. Two blast furnaces are simulated: a 9 m³ LKAB experimental BF with 3 tuyeres^[57] and a 5000 m³ industrial BF with 40 tuyeres. For the industrial BF (see Figure 2), two cases are considered: Case I is simulated by the integrated model and Case II is simulated by the process sub-model alone. Coal combustion is not modeled explicitly in Case II. Instead, the burnout is first determined using the statistical result of the raceway sub-model, the value of which equals 0.67 in this work. Then, the reducing gas conditions at the tuyere are determined *via* the local mass and heat balance, in which the burnout needs to be known. The reducing gas consists of CO 37.05 pct, N₂ 62.95 pct in molar percentage and has a temperature of 2,062 °C (2335K) in Case II. By contrast, the reducing gas condition is directly obtained by the raceway combustion model in Case I.

Table III. Simulation Conditions Used in the Present Study

	Industrial BF	LKAB Experimental BF
Productivity	2.2 [t/m ³ /day]	4 [t/m ³ /day]
Blast Rate	7200 [Nm ³ /min]	26.425 [Nm ³ /min]
Blast Temperature	1503 [K] (1230 °C)	1402 [K] (1129 °C)
O ₂ Enrichment	2 pct	5.9 pct
Top Pressure	230 [kPa]	150 [kPa]
PCI Rate	185 [kg/tHM] @ 318 [K] (45 °C) C 0.871 [mass pct]	130[kg/tHM]@ 318 [K] (45 °C) C 0.829 [mass pct]
Coke Ratio	302 [kg/tHM]	450[kg/tHM]
Slag Rate	254 [kg/tHM]	278.8 [kg/tHM]
Ore Composition	TFe 58.37, FeO 9.11 [mass pct]	TFe 57.7, FeO 9.23 [mass pct]
Ore Voidage	$0.403(100d_{ore})^{0.14}$	
Coke Voidage	$0.153\log(d_{coke}) + 0.724$	
Hot Metal Composition	C 0.04; Fe 0.96 [mass frac]	

Table IV. Coal Properties Used in the Present Study

Proximate Analysis (ad)	
Moisture	8.45 pct
Ash	8.73 pct
Volatile Matter	18.01 pct
Fixed Carbon	64.8 pct
Ultimate Analysis (daf.)	
C	81.69 pct
H	3.51 pct
O	5.27 pct
Gross Calorific Value (ad)	30.08 [kJ/kg]

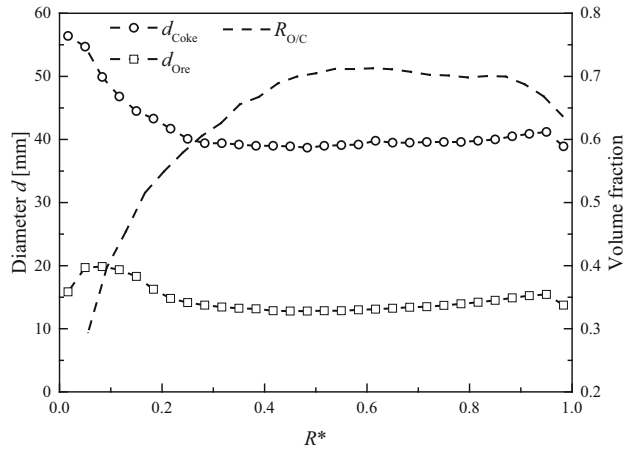


Fig. 3—Burden distribution for the industrial BF case.

C. PCI Conditions

Table IV lists the coal property used for the industrial BF in the current study. The particle size distribution is assumed to obey the Rosin-Rammler distribution, of which the mean size is 65 μm . The conveying gas (100 pct N₂) is 2,304 Nm³/h, while the corresponding coal rate and oxygen enrichment are 185 kg/tHM and 2 pct, respectively. The porosity in the raceway cavity and coke bed is set to 1 and 0.4, respectively.

D. Burden Conditions

Figure 3 shows the radial profiles of coke size (d_{Coke}), ore size (d_{Ore}), and ore-to-coke ratio ($R_{\text{O/C}}$) at the burden surface in the throat for the industrial BF. In the literature, the ore-to-coke ratio may be calculated according to two different definitions. One is the volume fraction of iron ore in the burden materials ($R_{\text{O/C,I}} = \frac{V_{\text{Ore}}}{V_{\text{Ore}} + V_{\text{Coke}}}$) and the other is the volume ratio of iron ore to coke layers ($R_{\text{O/C,II}} = \frac{V_{\text{Ore}}}{V_{\text{Coke}}}$). In this study, the first definition is used and can be converted into the second one by $R_{\text{O/C,II}} = \frac{R_{\text{O/C,I}}}{1 - R_{\text{O/C,I}}}$. For the LKAB experimental BF, the ore-to-coke ratio used is estimated from the measured CZ layer structures, while the coke and ore particle sizes are assumed to be uniform and set to 23 and 10.5 mm, respectively.

E. Tapping Conditions

The drainage process is assumed to be continuous at a fixed liquid level. The data of the liquid hot metal flow and temperature at the slag surface are extracted from the process sub-model predictions of the mixture of slag and hot metal and used as inlet conditions in modeling the hot metal flow and temperature fields in the hearth.^[50] The liquid density, thermal conductivity, and viscosity are assumed to be a function of hot metal temperature and calculated according to equations: $6825.5 - 0.50025*(T_{\text{HM}} - 1823)$, $0.0158T_{\text{HM}}$, and $(3.699 \times 10^{-4})e^{\frac{41,400}{R \times T_{\text{HM}}}}$, respectively.

IV. RESULTS AND DISCUSSION

A. Model Validation

The validity of the raceway combustion model and the hearth flow and heat transfer model has been verified elsewhere.^[10,49,50,55] Therefore, the current validation focuses on the process model and the integrated model through two different cases.

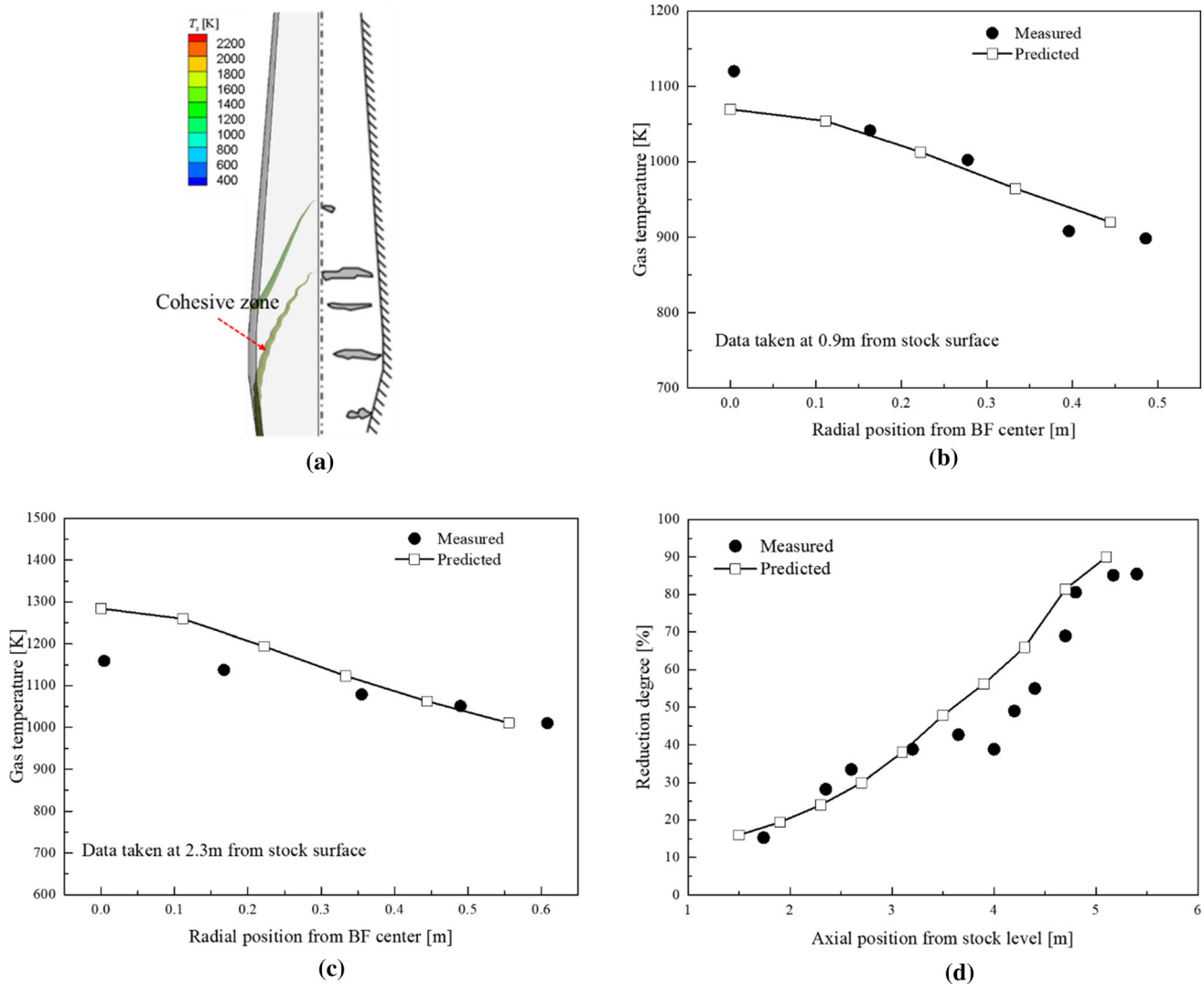


Fig. 4—Comparison of the calculated and measured results of LKAB BF in terms of (a) CZ profile, (b) gas temperature at the upper probe, (c) gas temperature at the lower probe, and (d) reduction degree.

First, the 9 m^3 LKAB experimental BF^[57] is considered to test the process model. Note that because of the lack of details about the raceway and hearth, the current work focuses on the process sub-model. In the experiments, two horizontal probes were used to measure the gas temperature in the radial direction at two different heights. Also, sampling baskets containing ore and coke were charged along with the batch. By quenching dissection, CZ shape and position were obtained and those sampling baskets were collected and analyzed to determine the axial profile of reduction degree. These results are considered for model validation here. Figure 4 shows that this process model can reasonably predict the in-furnace states such as the CZ position and shape, the gas temperature, and the reduction degree. Also, Table V shows that the predicted and measured performance indicators, including adiabatic temperature, top gas utilization factor, and top gas temperature are in good agreement, with the maximum value being less than 5.7 pct.

Secondly, the 5000 m^3 industrial BF is simulated by both the process sub-model and the integrated model. Only the overall performance indicators are considered in this validation as the in-furnace states are not available for this BF. Table VI demonstrates that both models can satisfactorily predict the measured top gas utilization factor/temperature, the productivity, and the tuyere pressure drop. Note that the process sub-model, if used alone, predicts the liquid temperature at the slag surface which is hence higher than the tapping temperature. The integrated model overpredicts the tapping temperature. One possible reason is that the hearth cooling system may not represent the real situation due to the lack of thermal couple data for reference. Nevertheless, all the results suggest that the current models are valid to study the BF ironmaking process, at least qualitatively.

Table V. Comparison of Measured and Predicted Performance Indicators of the LKAB Experimental BF

	Measured ^[57]	Predicted	Error
Adiabatic Temperature	2491 [K] (2213 °C)	2478 [K] (2200 °C)	-0.52 pct
Top Gas Utilization Factor	42.4 pct	43.1 pct	1.65 pct
Top Gas Temperature	493 [K] (220 °C)	521 [K] (248 °C)	5.7 pct

Table VI. Comparison of Simulated and Measured Performance Indicators of the 5000 m³ BF

Key Parameters	Plant Measurement	Simulation Results	
		Case I (Integrated Model)	Case II (Process Model)
Productivity	2.2 [t/m ³ /day]	2.23 [t/m ³ /day]	2.2 [t/m ³ /day]
Top Gas Temperature	453-513 [K] (180 °C to 240 °C)	450 [K] (177 °C)	449.6 [K] (171.6 °C)
Top Gas Utilization Factor	51.5 pct	53.8 pct	52.7 pct
HM Temperature	1788 [K] (1515 °C)	1821 [K] (1548 °C) at the taphole	1835 [K] (1562 °C) at the slag surface

B. In-furnace Features within Raceway, Main Body, and Hearth

The in-furnace states of the entire 5000 m³ industrial BF are examined by the integrated model using the results in Case I, which covers the raceway, the main body, and the hearth regions. For comparison, the results obtained by the process model in Case II without the integration are also shown. As discussed previously, the reducing gas conditions in the raceway region in Case I are given by the raceway combustion model. However, they are determined by local mass and energy conservation and are imposed at the gas inlet in Case II, assuming that the coal/coke combustion is completed inside the raceway. Besides, the mass and temperature distributions of the liquid at the slag surface in the hearth model are given by the process model in Case I, other than assumed in the hearth models that are used individually.^[49, 50] Table VII lists the main differences between Case I and Case II.

1. Raceway region

Figures 5 and 6 show the flow pattern and the burnout of coal particles in the raceway region. Here, the burnout represents the burning efficiency of coal particles, and the closer to 1 the value, the higher the burning efficiency. Overall, the phenomena in the raceway predicted by the integrated model are consistent with those obtained by a raceway sub-model alone.^[7,10,58,59] In particular, the phenomena have the following features. First, a recirculation vortex is present in the upper zone of the raceway (Figure 5(a)). Correspondingly, after being injected from the blowpipe, the blast flow keeps forward until a sharp turn at the endpoint of the raceway, and the velocity magnitude decreases dramatically as the blast enters the coke bed.

Consequently, the smaller coal particles that are carried by the gas are more likely to be captured by the vortex in which a higher burnout is anticipated, while the rest tends to keep forward due to the inertia, leading to shorter residence time and, thus, a lower burnout (Figure 5(b)).

Secondly, the coal combustion and the corresponding reducing gas distributions show anisotropic characteristics because of the recirculation vortex, as shown in Figure 6. As seen from this figure, the gas species (including O₂, CO and CO₂) and the temperature show a remarkable difference between the main coal plume and the recirculation zone. After a short period of pre-heating, considerable gaseous VM is generated. The combustion of VM goes faster than char/coke combustion, leading to a dramatic increase in CO₂ content and a sharp decrease in O₂, and, thus, a remarkable rise in temperature along the coal plume. Then, the remaining O₂ and CO₂ are converted into CO by char/coke gasification reactions. Therefore, the CO appears to be lean along the plume. By contrast to the plume zone, the recirculating zone has a higher CO content due to longer residence time and fewer VM generation.

Here, it should be pointed out that the three-dimensional strongly anisotropic flow and combustion details, as demonstrated in Case I, cannot be incorporated into a process model that does not explicitly include the raceway model, *e.g.*, in Case II. Moreover, when the combustion model is omitted from a process model, the coal burnout must be assumed constant. Additionally, in Case I, to be computationally efficient, the results given by the combustion model are passed on to the process sub-model in a one-way scheme and, thus, are not affected by the model integration.

Table VII. Comparison of Case I and Case II

Key Features	Case I	Case II
	Model	integrated model consisting of process sub-model, raceway sub-model and hearth sub-model
Computational Domain	burden surface to hearth bottom including raceway	burden surface to slag surface
Reducing Gas Condition	predicted by the raceway sub-model	the burnout is obtained by the raceway sub-model, and then reducing gas component and temperature are determined using local heat and mass balance
Coke Combustion and Gasification in the Dripping Zone	considered	coke combustion and gasification are assumed to be completed in the raceway
Coal Combustion	modeled explicitly	modeled implicitly
Hearth Flow and Heat Transfer	yes	no

2. Main body region

Figure 7(a) presents the blast flow streamlines, colored by blast velocity magnitudes, where the CZ is also shown. The CZ is defined corresponding to the solid temperature between 1473 K (1200 °C) as the softening temperature and 1673 K (1400 °C) as the melting temperature. The ore is assumed to melt down completely at the lower CZ boundary. As seen in Figure 7(a), the blast after leaving the raceway is re-arranged by the CZ that acts as a distributor and eventually achieves an even distribution at the upper part of the BF. Expectedly, a rapid change in the flow direction of the blast is observed in the CZ. This is due to the anisotropic behavior of the bed permeability inside this zone resulting from ore melting, as reflected by the porosity distribution shown in Figure 7(c). Besides, the CZ in Case I is flatter compared to case II. This is because only the former considers the fact that more blast is entrained to the wall side by the recirculation vortex, and less heat is brought up to the center. Consequently, the temperature in Case I is lower at the center and higher near the wall, leading to a flatter CZ.

Figures 7(d) and (e) show the spatial distributions of liquid volume fraction and superficial velocity for different models. A stronger liquid flow develops near the wall, corresponding to the higher O/C ratio there. Because of the low permeability of the deadman, the liquid holdup is generally higher in the deadman compared to the dripping zone. The liquid superficial velocities are generally larger near the raceway, which is caused by the reduced cross-sectional area when the liquid passes through the surface of the raceway cavity. Although the recirculating vortex, which is considered in the integrated model, affects liquid and gas flows, its effect on the liquid flow appears minor. Therefore, the liquid volume fraction and velocity distributions predicted by the two models are similar.

Figures 8(a) and (b) present the CO and CO₂ distributions. These predicted distributions by the integrated model in Case I are similar to those given by the process sub-model alone in Case II. This trend also applies to the distributions of gas utilization factor $\left(\frac{CO_2}{CO_2 + CO}\right)$ in Figure 8(c), reduction degree in Figure 8(d), indirect reaction rate in Figure 8(e), and gas and solid temperature in Figures 8(g) and (h). Here, the reduction degree f_s is defined as the ratio of the lost oxygen during the reduction to the total oxygen in hematite and calculated by $1 - \frac{W_o}{W_{Fe}} \times \frac{112}{48}$, where W_{Fe} and W_o are, respectively, the mass fractions of the iron in the ore fed into the furnace and the oxygen combined with the iron after the reduction. However, the CO concentration is relatively higher near the center because of the strong reducing environment resulting from the lower O/C ratio there. In Case I, this effect is somewhat mitigated by the effect of circulating vortex. Correspondingly, the gas utilization factor and the reduction degree become slightly weaker in the central area.

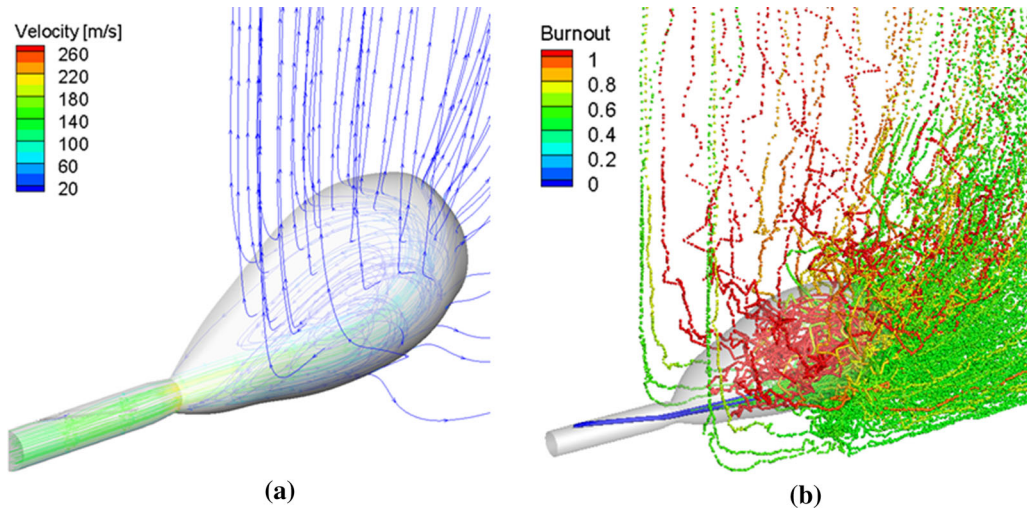


Fig. 5—(a) Gas-particle flow pattern and (b) coal burnout in the raceway region.

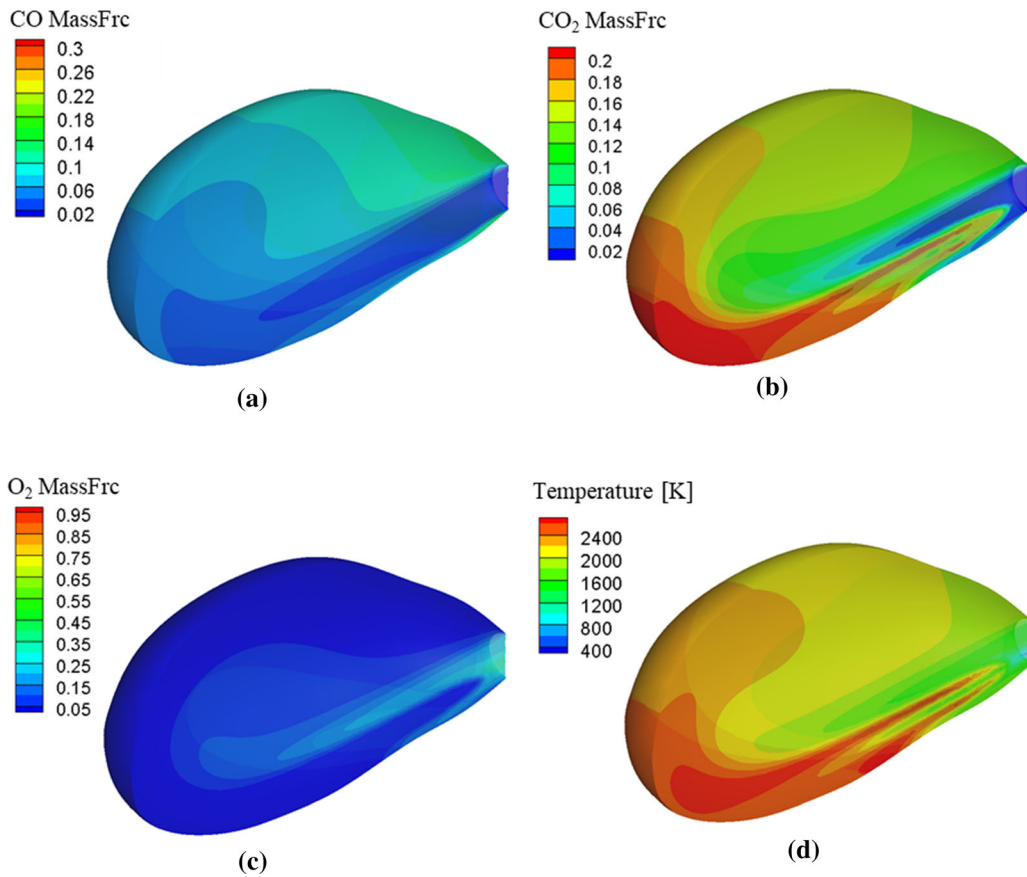


Fig. 6—Blast composition and temperature profiles inside the raceway: (a) CO mass fraction, (b) CO₂ mass fraction, (c) O₂ mass fraction, and (d) temperature.

To be quantitative in the analysis, the reducing gas components at the tuyere level in Case I are plotted against the distance away from the center in Figure 9. As seen from this figure, along the coal plume, the generation of CO₂ is earlier than CO because of the combustion of VM, which leads to the fast depletion of

oxygen. Because of char/coke solution loss reaction, CO₂ concentration reaches its maximum in the vicinity of the front surface of the raceway, where CO starts to increase rapidly. This is consistent with the result shown in Figure 6 that demonstrates strong anisotropic characteristics of combustion in the raceway. Note that the

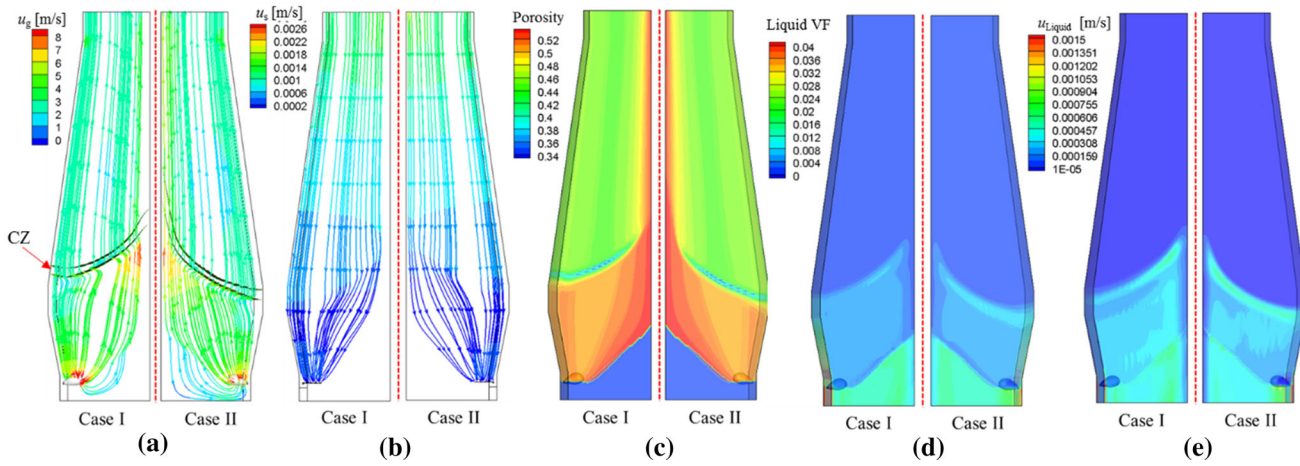


Fig. 7—(a) Gas flow streamlines and spatial distributions, (b) solid streamlines, (c) bed porosity, (d) liquid volume fraction, and (e) liquid superficial velocity.

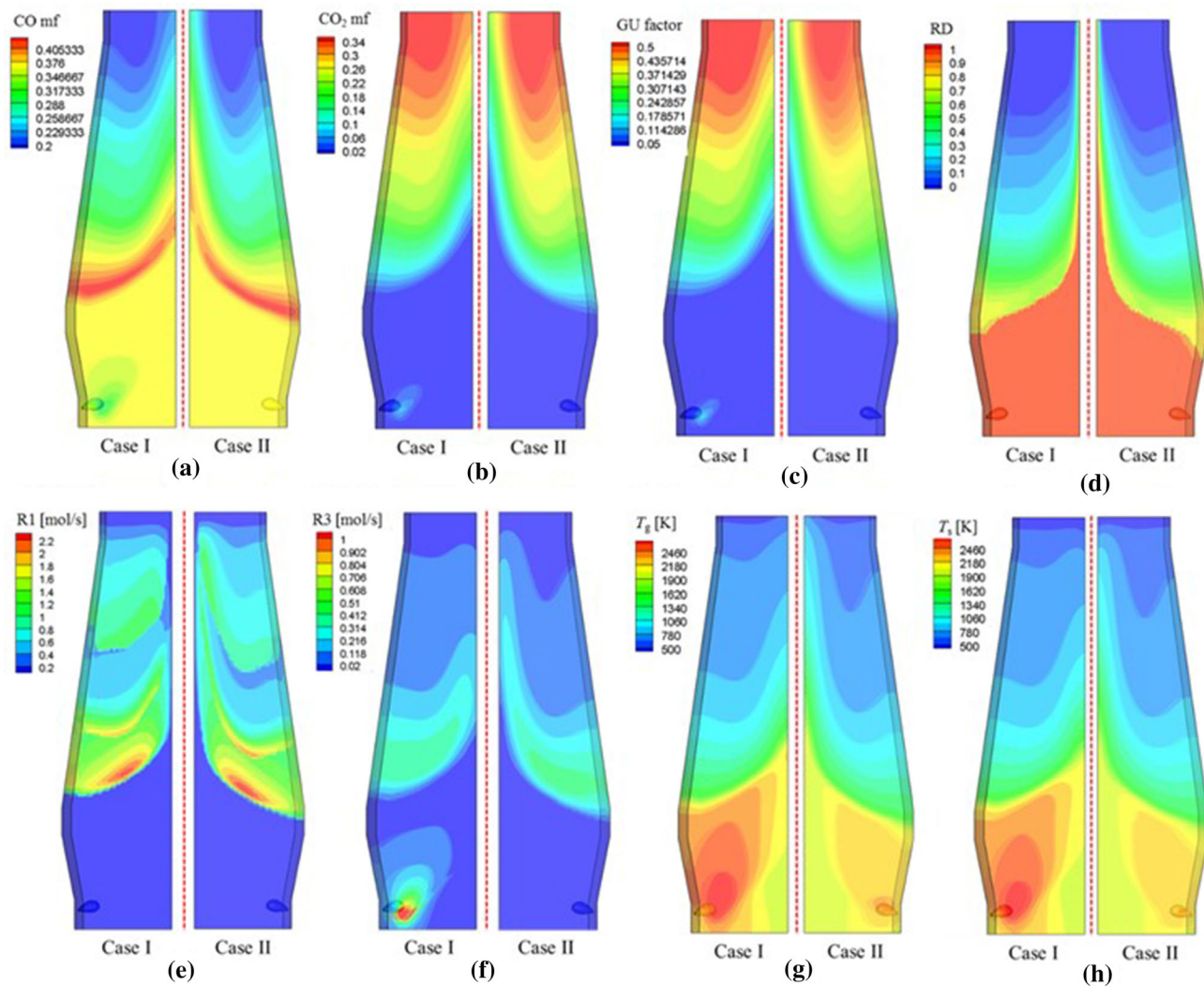


Fig. 8—(a) CO mass fraction, (b) CO₂ mass fraction, (c) gas utilization factor, (d) reduction degree, (e) indirect reduction rate, (f) carbon solution loss rate, (g) gas temperature, and (h) solid temperature.

reducing gas leaving the raceway is a mixture of CO, CO₂, O₂ and N₂ (Figure 6). The remaining oxygen continues to combust with coke particles, while the “Boudouard reaction” or “carbon solution reaction” converts CO₂ into CO. Such a phenomenon is modeled in Case I but neglected in Case II. It can be further supported by the reaction rate of carbon solution shown in Figure 8(f), where the rate in the nearby region outside the raceway is significant in Case I but equals zero in Case II. Because O₂ and CO₂ still exist in the blast in the nearby region outside the raceway in Case I, the exothermic coke combustion and the endothermic Boudouard reaction both occur there, the rates of which are calculated *via* the same correlations applied in the raceway (see Table II). Thus, the gas and solid temperatures increase initially and then decrease dramatically in the dripping zone. This phenomenon is not observed

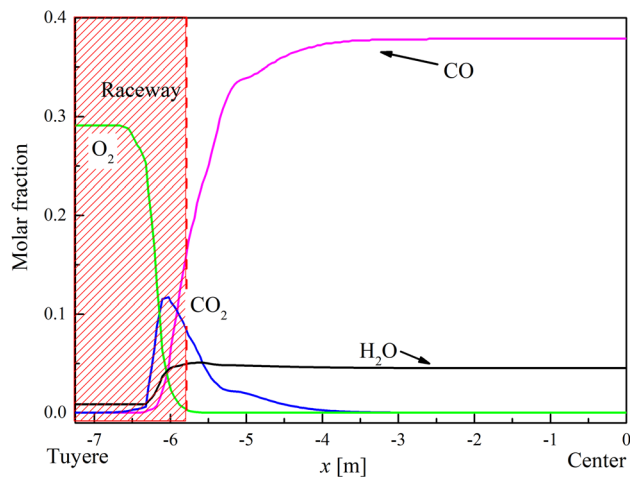


Fig. 9—Radial profiles of gas compositions at the tuyere level.

in Case II, as shown in Figures 8(g) and (h). These figures also show that the gas and solid temperatures are more uniform in the radial direction in Case I than Case II as only the former considers the recirculating vortex inside the raceway and the carbon solution outside the raceway. Consequently, the CZ is more inclined in Case II.

3. Hearth region

Figure 10 shows the predicted liquid temperature contours and the flow streamlines by the hearth model integrated with the process model. Overall, the results are consistent with those obtained *via* the hearth sub-model alone by Guo *et al.*^[49] and Komiyama *et al.*,^[50] who specified the inlet profiles of liquid velocity and temperature according to empirical experience. There are a few features observed. First, two stratified layers are identified with a nearly flat interface located below the taphole level. Correspondingly, two regions with distinct flow patterns are observed. One is the active region in the upper part, where the velocity is relatively greater. The other is the pseudo-stationary region at the bottom where the hot metal keeps almost stationary. Secondly, the natural convection is present in the active region resulting from the temperature difference in the vertical direction. Notably, the liquid temperature in the upper region shows a strongly anisotropic characteristic in both horizontal and vertical directions, and this non-uniformity extends down to the taphole level, affecting the tapping temperature of hot metal. By contrast, a nearly uniform temperature profile was observed in the previous studies^[49,50] in which the liquid was assumed to be absent in the central area and uniformly distributed in the peripheral area with a constant temperature. Nevertheless, the horizontal

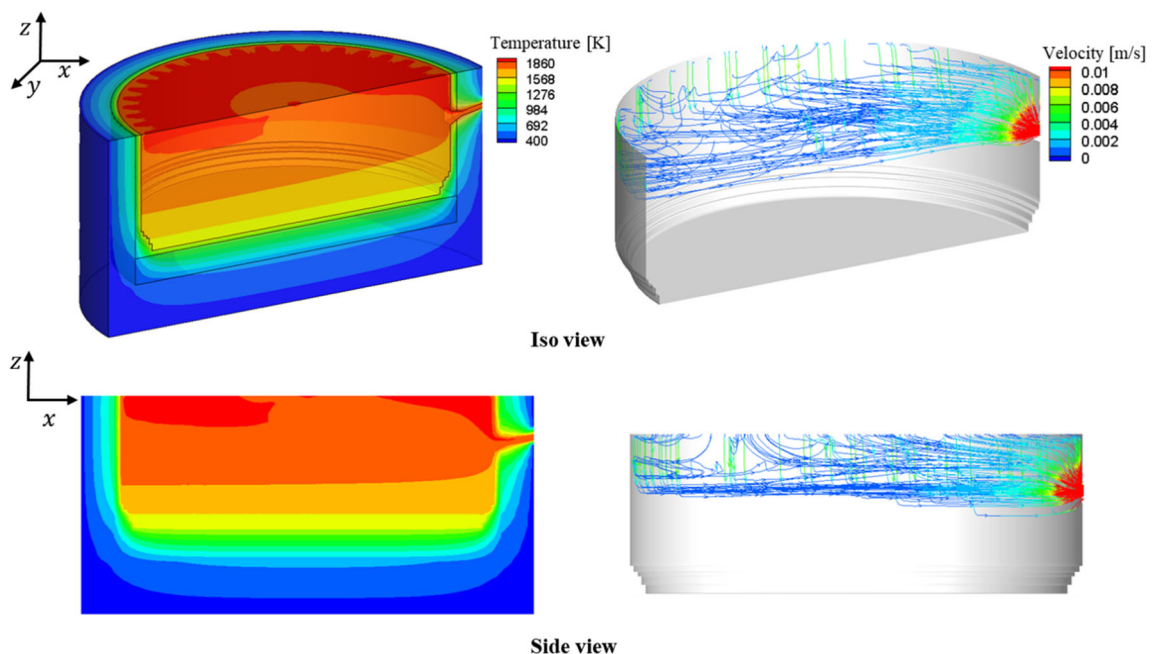


Fig. 10—Hot metal flow and thermal conditions inside the hearth in Case I.

layers of temperature isothermals in the lower region are

found similar in the current and previous studies. In this region, the temperature gradient almost exits vertically.

C. Influence of Burden Distribution

Burden distribution significantly affects the efficiency and reliability of BF. It has been extensively studied numerically^[42,60–62] and experimentally.^[63–66] The previous studies focus on the particle motion in the top charging system and the burden distribution in the throat. To date, our knowledge about the influence of burden distribution on the in-furnace states, especially in the hearth, is very limited. As an example to demonstrate its usefulness, the current integrated model studies this influence.

Here, five top burden distributions in the throat as shown in Figure 11 are inputted into the integrated model for conducting numerical experiments. Their difference lies in the radial profile of O/C ratio, given by $R_{O/C} = \left(\frac{V_{ore}}{V_{ore} + V_{coke}} \right)$. For simplicity, $R_{O/C}$ is assumed to vary linearly with the dimensionless radius R^* and is described by $R_{O/C} = A + BR^*$. Provided that the sum of

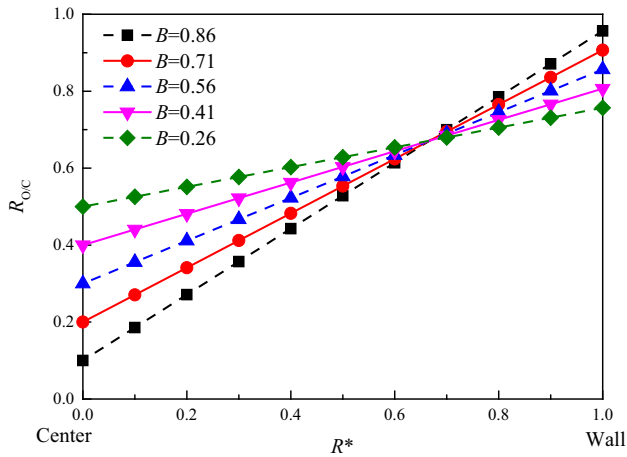
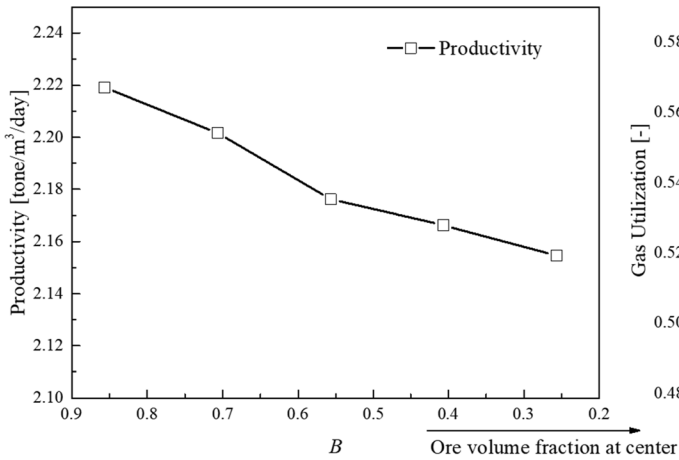
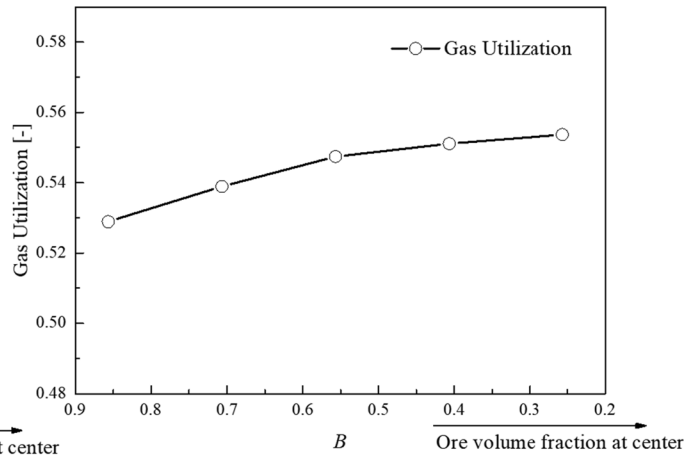


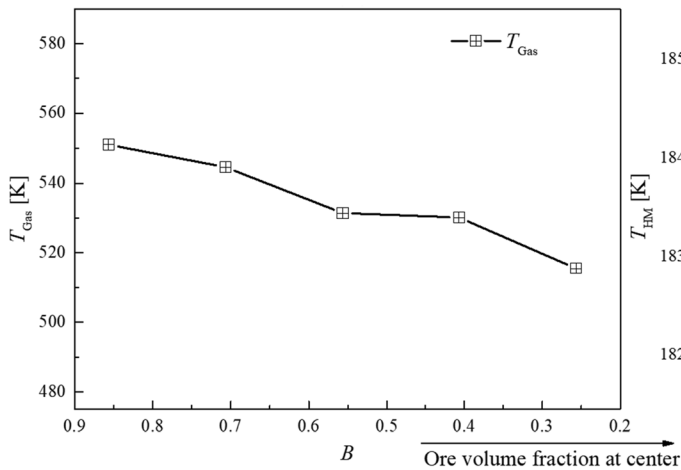
Fig. 11—Different burden distribution profiles at the burden surface in the throat.



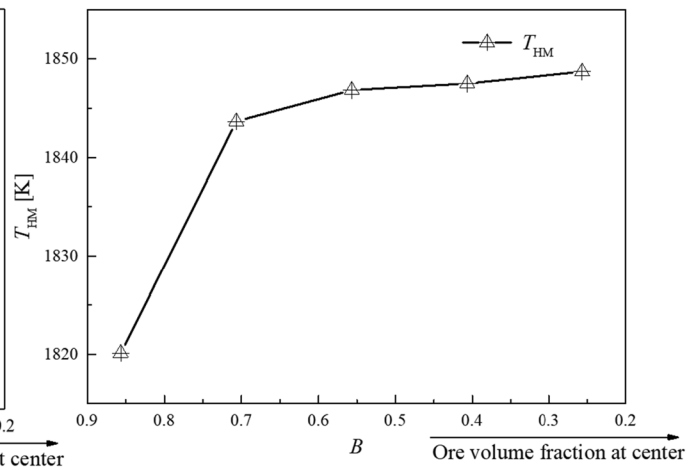
(a)



(b)



(c)



(d)

Fig. 12—BF overall performance under various burden distribution patterns: (a) productivity [tone/m³/day], (b) top gas utilization factor, (c) off-gas temperature [K], and (d) hot metal temperature at the taphole [K].

$R_{O/C} = \int_0^1 R_{O/C} dR^*$ in the radial direction equals 0.671, the value of A is set to 0.1, 0.2, 0.3, 0.4, and 0.5, respectively. Correspondingly, the value of B is determined as 0.86, 0.71, 0.56, 0.41, and 0.26, respectively, for maintaining the constant coke rate of 300 kg/tHM. As B decreases, the top burden distribution changes from a more “center coke developed” mode to a “uniform” one. In the simulations, the ore diameter is set to 30 mm, while the coke size is described by $d_{\text{Coke}} = 60 - 30R^*$ (mm).

Figure 12 demonstrates how burden distribution affects BF performance. With decreasing B , the productivity decreases while the top gas utilization factor increases, similar to the observations by others.^[60,64] Note that the fuel ratio is kept constant in this study. Under this configuration, a larger top gas utilization factor indicates a higher potential in reducing the fuel rate. The better gas utilization in a more uniform burden distribution, as shown in Figure 12, is attributed to the better contact between the reducing gas and the solid materials. Consequently, the indirect reduction is favored while the direct reduction tends to be prohibited. When the carbon consumption by the direct reduction decreases, the productivity must decrease to meet the overall carbon mass balance while keeping a

constant fuel ratio. For the same reason, the off-gas temperature decreases from 551 K (278 °C) in the most center-developed case to 515 K (242 °C) in the most uniform case. Conversely, the hot metal temperature at the taphole shows an opposite trend. With decreasing B , the hot metal temperature increases rapidly first and then slowly.

Figure 13 compares the internal states in the main body region with respect to different top burden distributions. A flatter CZ is observed as the uniformity of radial burden distribution is enhanced. Accordingly, the internal thermochemical distributions that are strongly affected by the CZ vary. In general, the indirect reduction rate and associated quantities become more evenly distributed as B decreases. Besides, the liquid holdup near the deadman is much lower in the most center-developed case than in the most uniform one, which can be evidenced by the liquid velocity and volume fractions contours plotted in Figures 13(d) and (f).

Figure 13(e) shows that as B decreases, the temperature increases near the wall; however, it decreases near the center because the permeability there is relatively low due to the existence of the deadman. It should be pointed out that although the deadman gets deactivated,

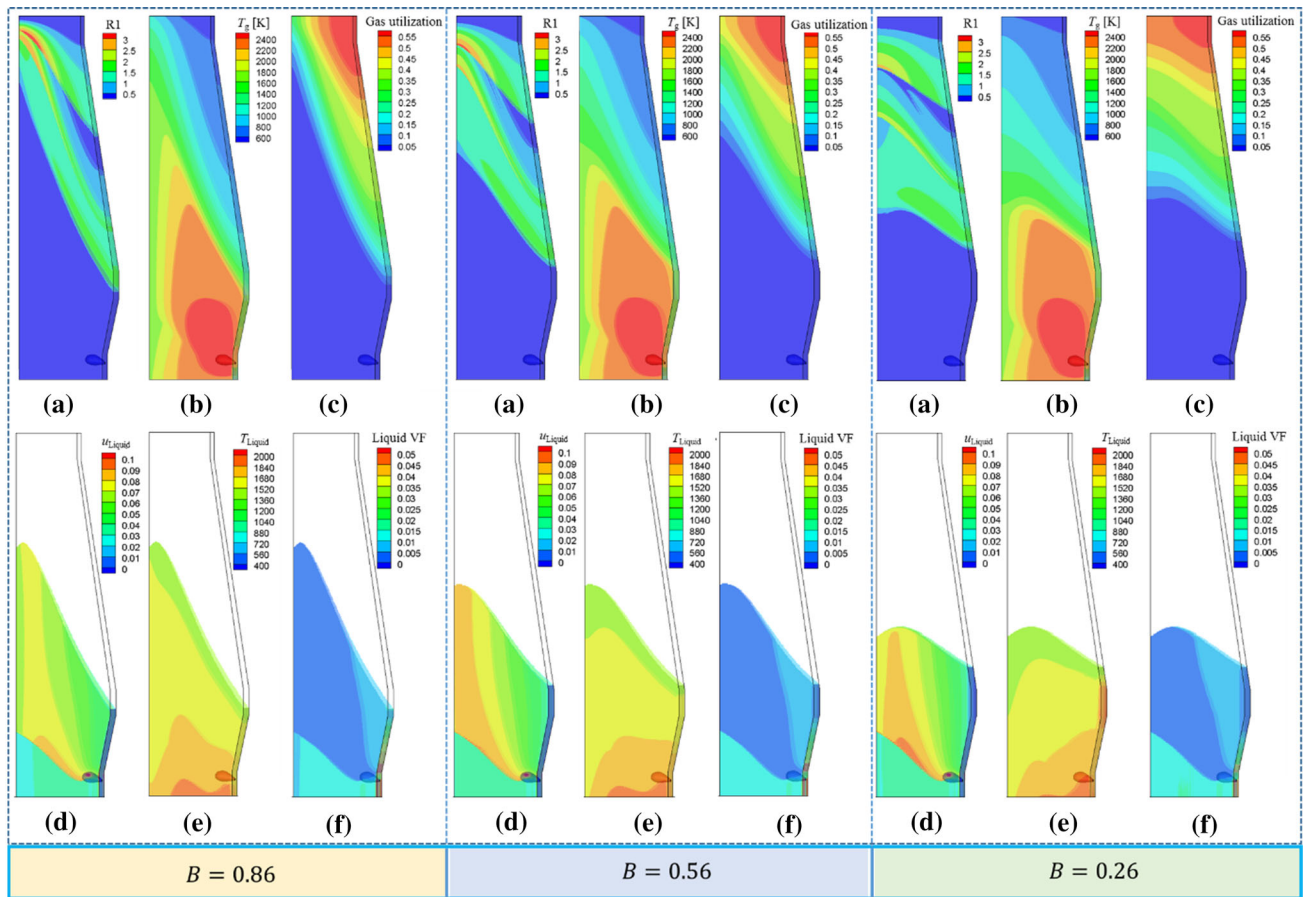


Fig. 13—In-furnace states under various burden distributions: (a) indirect reduction rate [mol/m³·s], (b) gas temperature [K], (c) gas utilization factor, (d) liquid velocity [m/s], (e) liquid temperature [K], and (f) liquid volume fraction.

the average temperature of the hot metal entering the hearth increases with the decrease of B , leading to an overall increase in liquid temperature in the hearth. In other words, the hot metal temperature becomes relatively uneven for a more uniform burden distribution.

The result in Figure 13 also helps explain the variation of liquid temperature with burden distribution shown in Figure 12. As B decreases, the endothermic direct reduction is prohibited while the productivity slightly drops, which saves more energy for heating up hot metal. On the other hand, at a large B (e.g., 0.86 here), the ore mainly concentrates near the wall. Thus, a strong liquid flow is developed near the wall (Figure 13(d)), leading to a substantial heat loss through the wall, as reflected from the relatively low temperature at the periphery (Figure 13(e)). Also, the CZ root at a large B is low, corresponding to a short distance for heating up hot metal. These two adverse effects are both migrated with decreasing B , intensifying the increase of hot metal temperature substantially. However, as B

continues to decline, the wall effect is less significant. Meanwhile, the CZ root ascends less apparently, whereas the CZ head continues to drop. The distance for heating up hot metal becomes shorter once the drop of the CZ head plays a dominant role. All these slow down the increase of hot metal temperature.

Figure 14 shows the distributions of hot metal flow and temperature inside the hearth. As the burden distribution shifts to a uniform pattern or B decreases, the temperature of hot metal becomes less uniform at the slag surface or the hearth entrance, while the flow is stronger in the central area (Figure 14(a)). Meanwhile, the temperature non-uniformity expands downwards from the slag surface to the hearth bottom, which is more obvious when the burden becomes uniform (Figures 14(b) and (c)). The active region gradually enlarges while the downwards velocity of hot metal near the wall decreases dramatically. Also, a downward jet featured with large velocity magnitudes is identified, which becomes more significant in the case of uniform

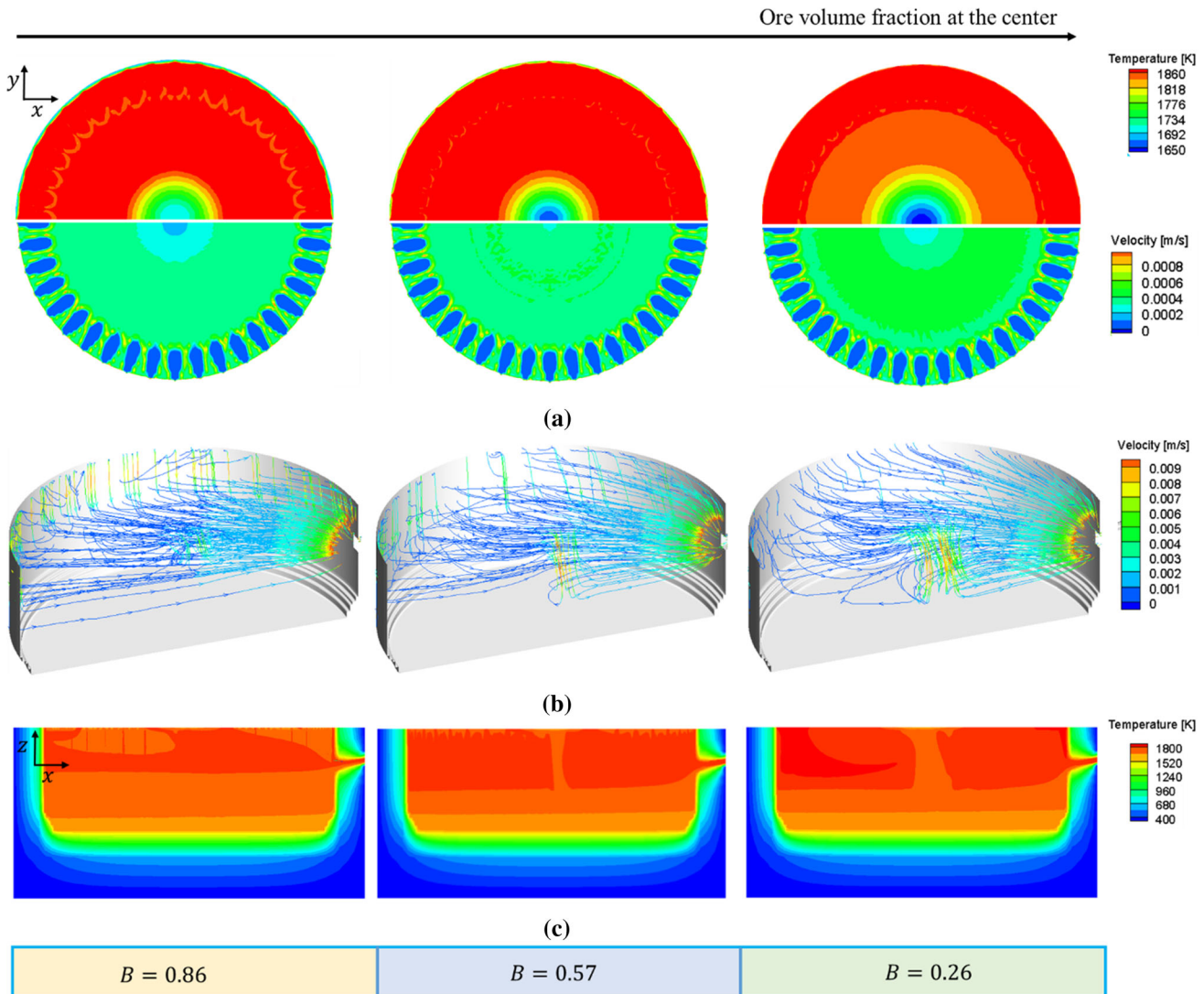


Fig. 14—Hot metal flow and thermal conditions inside the hearth under various burden distributions: (a) temperature (upper) and velocity (lower) profiles at the slag surface, (b) streamlines of the hot metal, and (c) temperature profile.

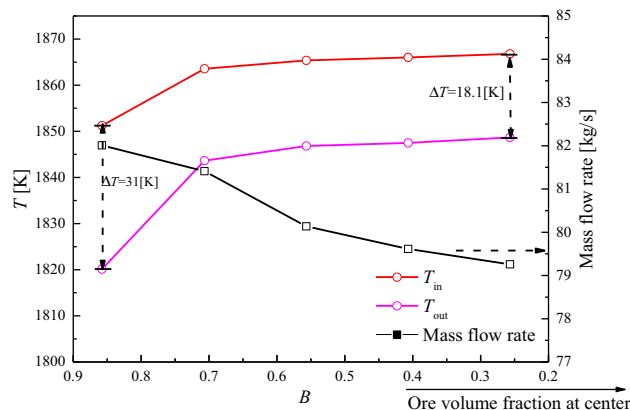


Fig. 15—Average hot metal temperature at the slag surface and the taphole as well as mass the flow rate under different burden distributions.

burden distribution. Such a jet is caused by the relatively low liquid temperature in the central area (see Figure 14(a)), which results in heavier liquid preferring to flow down. It promotes the mixing and the follow ability in the hearth, which helps reduce the non-uniform temperature distribution of hot metal. It should be pointed out that for simplicity, the current modeling does not consider the slag flow in the hearth. This jet effect could be practically weaker as the relatively low temperature near the hearth center increases the slag viscosity and decreases the flowability.

Figure 15 plots the liquid temperature at the slag surface and the taphole for different burden distributions. Overall, the two temperatures show a similar trend and their difference decreases from 31 K in the most center-developed case to 18.1 K in the most uniform one. This is attributed to the smaller heat loss through the hearth refractories resulting from the reduced downward velocities near the wall as the uniformity of burden distribution increases. This decrease in the liquid velocity near the wall also helps mitigate the erosion of refractories. However, as discussed previously, a more uniform burden distribution causes lower liquid temperatures in the central area and thus a more non-uniform distribution on cross-sectional areas. Therefore, a uniform burden distribution may be modified by loading more coke into the central area,^[60] so that the gas flow can be more centrally developed, which enables bringing more heat or energy into the central area for heating up the burden material and liquid. In this way, the non-uniformity of liquid temperature can be mitigated, while the benefits of uniform burden distribution in reducing wall heat loss and erosion as well as in increasing reducing gas utilization can be maintained.

V. CONCLUSION

In this work, based on ANSYS CFX, an integrated BF process model covering from the top burden surface down to the bottom of the hearth has been developed to describe the entire BF ironmaking process. It is done by

incorporating our well-established raceway model and hearth model into our process model through shared libraries. This integration eliminates the assumptions at boundaries between different sub-models and can directly link the model to different operating parameters. The applicability of the integrated model has been verified by the reasonable agreement between measured and predicted results in terms of in-furnace states and overall performance.

The comparison of the integrated model and the process sub-model shows that the two models predict similar in-furnace states in the main body region and the overall BF performance. However, a fatter cohesive zone is predicted by the integrated model because it considers the recirculating vortex and the anisotropic combustion behaviors of pulverized coal and coke bed in the raceway region and the continuing combustion of coke in the nearby region outside the raceway.

The study of top burden distribution by the integrated model shows that as the burden distribution shifts from the center-developed mode to the uniform one, the cohesive zone gradually becomes flat. The utilization efficiency of gas and the tapping temperature of liquid iron show an increasing trend, while the off-gas temperature and productivity drop. Meanwhile, the hot metal temperature near the deadman center drops, but the average temperature of the liquid entering the hearth rises. Therein, a downward jet near the hearth center is observed due to the buoyancy force induced by temperature difference. Also, the active zone inside the hearth enlarges and a better mixing state inside hearth develops due to the collective effect of the elevation in average hot metal temperature and the reduction in wall heat loss.

ACKNOWLEDGMENTS

The authors are grateful to the Australian Research Council (Grant No. IH140100035), the Natural Science Foundation of China (Grant No. U1560205), and National Key R&D Program of China (Grant No. 2017YFB0304304) for the partial financial support of this work, and the China Scholarship Council (CSC) for Liu (Grant No. 201708510077) and the Australian National Computational Infrastructure for the high-performance computation.

NOMENCLATURE

ABBREVIATIONS

A_p	Particle area (m^2)
C	Specific heat ($J/kg\ K$)
C_D	Drag coefficient
D	Abbreviation of Dynamic
d	Diameter (m)
f	Interphase force (N/m^3)

g	Gravitational acceleration (m/s ²)
I	Radiation intensity on particle surface (w/m ²)
m_p	Particle mass (kg)
Nu	Nusselt number
R	Resistance force (N/m ³)
R^*	Dimensionless radial distance
S	Source term
Sh	Shrinkage ratio
T	Temperature (K)
U	True Velocity (m/s)
VM	Volatile matter

GREEK LETTERS

β	Thermal coefficient of volumetric expansion (1/K)
Γ	Diffusion coefficient
ε	Volume fraction
ε_p	Particle emissivity
λ	Thermal conductivity (W/m K)
ρ	Density (kg/m ³)
σ_B	Stefan-Boltzmann constant 5.67×10^8 (W/m ² K ⁴)
τ	Stress tensor (Pa)
\emptyset	General variable

SUB/SUPERSCRIPTS

g	Gas phase
ad	Air dried based
daf	Dried ash free based
i	i th phase
l	Liquid phase
p	Particle phases
s	Solid phase

REFERENCES

- S. Kuang, Z. Li, and A. Yu: *Steel. Res. Int.*, 2018, vol. 89, pp. 1700071–96.
- X. Dong, A. Yu, J.-I. Yagi, and P. Zulli: *ISIJ Int.*, 2007, vol. 47, pp. 1553–70.
- J.-I. Yagi: *ISIJ Int.*, 1993, vol. 33, pp. 619–39.
- S. Ueda, S. Natsui, H. Nogami, J.-I. Yagi, and T. Ariyama: *ISIJ Int.*, 2010, vol. 50, pp. 914–23.
- T. Ariyama, S. Natsui, T. Kon, S. Ueda, S. Kikuchi, and H. Nogami: *ISIJ Int.*, 2014, vol. 54, pp. 1457–71.
- T. Okosun, A.K. Silaen, and C.Q. Zhou: *Steel. Res. Int.*, 2019, vol. 90, pp. 1900046–62.
- H. Nogami, H. Yamaoka, and K. Takatani: *ISIJ Int.*, 2004, vol. 44, pp. 2150–58.
- S. Yuu, T. Umekage, and T. Miyahara: *ISIJ Int.*, 2005, vol. 45, pp. 1406–15.
- M. Gu, G. Chen, M. Zhang, D.F. Huang, P. Chaubal, and C.Q. Zhou: *Appl. Math. Model.*, 2010, vol. 34, pp. 3536–46.
- Y. Shen, B. Guo, A. Yu, P. Austin, and P. Zulli: *Fuel*, 2011, vol. 90, pp. 728–38.
- K. Nishioka, T. Maeda, and M. Shimizu: *ISIJ Int.*, 2005, vol. 45, pp. 1506–14.
- L. Shao and H. Saxén: *ISIJ Int.*, 2011, vol. 51, pp. 228–35.
- M. Zagaria, V. Dimastromatteo, and V. Colla: *Ironmak. Steelmak.*, 2010, vol. 37, pp. 229–34.
- L. Shao and H. Saxén: *Steel. Res. Int.*, 2012, vol. 83, pp. 878–85.
- C.Q. Zhou, F. Huang, Y. Zhao, and P. Chaubal: *J. Therm. Sci. Eng. Appl.*, 2010, vol. 2, p. 011006.
- V. Panjkovic, J. Truelove, and P. Zulli: *Ironmak. Steelmak.*, 2002, vol. 29, pp. 390–400.
- W. Cheng, E. Huang, and S. Du: *Int. Commun. Heat. Mass*, 2014, vol. 57, pp. 13–21.
- H. Nogami and J.-I. Yagi: *ISIJ Int.*, 2004, vol. 44, pp. 1826–34.
- J. Chen, T. Akiyama, H. Nogami, J.-I. Yagi, and H. Takahashi: *ISIJ Int.*, 1993, vol. 33, pp. 664–71.
- Z. Zhou, A. Yu, and P. Zulli: *Prog. Comput. Fluid Dy.*, 2004, vol. 4, pp. 39–45.
- S. Zhang, A. Yu, P. Zulli, B. Wright, and U. Tüzün: *ISIJ Int.*, 1998, vol. 38, pp. 1311–19.
- P. Austin, H. Nogami, and J.-I. Yagi: *ISIJ Int.*, 1997, vol. 37, pp. 748–55.
- H. Nogami, Y. Kashiwaya, and D. Yamada: *ISIJ Int.*, 2012, vol. 52, pp. 1523–27.
- S. Natsui, T. Kikuchi, and R.O. Suzuki: *Metall. Mater. Trans. B*, 2014, vol. 45B, pp. 2395–413.
- S.J. Chew, P. Zulli, and A. Yu: *ISIJ Int.*, 2001, vol. 41, pp. 1112–21.
- G. Wang, S.J. Chew, A. Yu, and P. Zulli: *Metall. Mater. Trans. B*, 1997, vol. 28, pp. 333–43.
- G. Wang, J.D. Litster, and A. Yu: *ISIJ Int.*, 2000, vol. 40, pp. 627–36.
- S. Natsui, T. Kikuchi, R.O. Suzuki, T. Kon, S. Ueda, and H. Nogami: *ISIJ Int.*, 2015, vol. 55, pp. 1259–66.
- S. Natsui, K.-I. Ohno, S. Sukenaga, T. Kikuchi, and R.O. Suzuki: *ISIJ Int.*, 2018, vol. 58, pp. 282–91.
- J.A.D. Castro, H. Nogami, and J.-I. Yagi: *ISIJ Int.*, 2000, vol. 40, pp. 637–46.
- Y. Hashimoto, Y. Sawa, Y. Kitamura, T. Nishino, and M. Kano: *ISIJ Int.*, 2018, vol. 58, pp. 2210–18.
- X. Dong, A. Yu, S. Chew, and P. Zulli: *Metall. Mater. Trans. B*, 2010, vol. 41B, pp. 330–49.
- K. Yang, S. Choi, J. Chung, and J.-I. Yagi: *ISIJ Int.*, 2010, vol. 50, pp. 972–80.
- P. Zhou, H.-L. Li, P.-Y. Shi, and C.Q. Zhou: *Appl. Therm. Eng.*, 2016, vol. 95, pp. 296–302.
- S. Kuang, Z. Li, D. Yan, Y. Qi, and A. Yu: *Miner. Eng.*, 2014, vol. 63, pp. 45–56.
- D. Fu, Y. Chen, Y. Zhao, J. D'Alessio, K.J. Ferron, and C.Q. Zhou: *Appl. Therm. Eng.*, 2014, vol. 66, pp. 298–308.
- L. Jiao, S. Kuang, A. Yu, Y. Li, X. Mao, and H. Xu: *Metall. Mater. Trans. B*, 2020, vol. 51B, pp. 258–75.
- X. Dong, S. Zhang, D. Pinson, A. Yu, and P. Zulli: *Powder Technol.*, 2004, vol. 149, pp. 10–22.
- J.A.D. Castro, S. Alexandre Jose Da, S. Yasushi, and J.-I. Yagi: *ISIJ Int.*, 2011, vol. 51, pp. 748–58.
- S. Natsui, R. Shibasaki, T. Kon, S. Ueda, R. Inoue, and T. Ariyama: *ISIJ Int.*, 2013, vol. 53, pp. 1770–78.
- Q. Hou and A. Yu: *AIChE J.*, 2016, vol. 62, pp. 4240–50.
- P. Austin, H. Nogami, and J.-I. Yagi: *ISIJ Int.*, 1997, vol. 37, pp. 458–67.
- J.A.D. Castro, H. Nogami, and J.-I. Yagi: *ISIJ Int.*, 2002, vol. 42, pp. 44–52.
- K. Takatani, T. Inada, and Y. Ujisawa: *ISIJ Int.*, 1999, vol. 39, pp. 15–22.
- S.J. Chew, P. Zulli, and A. Yu: *ISIJ Int.*, 2001, vol. 41, pp. 1122–30.
- Z. Li, S. Kuang, D. Yan, Y. Qi, and A. Yu: *Metall. Mater. Trans. B*, 2017, vol. 48B, pp. 602–18.
- Y. Shen, B. Guo, S.J. Chew, P. Austin, and A. Yu: *Metall. Mater. Trans. B*, 2014, vol. 46B, pp. 432–48.
- T. Inada, K. Takata, K. Takatani, and T. Yamamoto: *ISIJ Int.*, 2003, vol. 43, pp. 1003–10.
- B. Guo, D. Maldonado, P. Zulli, and A. Yu: *ISIJ Int.*, 2008, vol. 48, pp. 1676–85.
- K.M. Komiyama, B. Guo, H. Zughbi, P. Zulli, and A. Yu: *Metall. Mater. Trans. B*, 2014, vol. 45B, pp. 1895–914.
- D. Fu, G. Tang, Y. Zhao, J. D'Alessio, and C.Q. Zhou: *JOM*, 2018, vol. 70, pp. 951–57.

52. T. Inada, K. Takatani, K. Takata, and T. Yamamoto: *ISIJ Int.*, 2003, vol. 43, pp. 1143–50.
53. K. Takatani, T. Inada, and K. Takata: *ISIJ Int.*, 2001, vol. 41, pp. 1139–45.
54. J. Liao, A. Yu, and Y. Shen: *Powder Technol.*, 2016, vol. 314, pp. 550–56.
55. B. Guo, P. Zulli, H. Rogers, J. Mathieson, and A. Yu: *ISIJ Int.*, 2005, vol. 45, pp. 1272–81.
56. S.-I. Nomura: *T. Iron Steel I. Jpn.*, 1986, vol. 26, pp. 107–13.
57. S. Watakabe, K. Miyagawa, S. Matsuzaki, T. Inada, Y. Tomita, K. Saito, M. Osame, P. Sikström, L. Ökvist, and J.-O. Wikstrom: *ISIJ Int.*, 2013, vol. 53, pp. 2065–71.
58. D.C. Sau, S.K. Das, G.K. Mandal, and D. Bandyopadhyay: *Int. J. Simul. Model*, 2018, vol. 38, pp. 232–42.
59. S. Matsuzaki, T. Nishimura, A. Shinotake, K. Kunitomo, M. Naito, and T. Sugiyama: *Nippon Steel Tech. Rep.*, 2015, vol. 90, pp. 87–96.
60. Z. Li, S. Kuang, S. Liu, J. Gan, A. Yu, Y. Li, and X. Mao: *Powder Technol.*, 2019, vol. 353, pp. 385–97.
61. S. Liu, Z. Zhou, K. Dong, A. Yu, D. Pinson, and J. Tsalapatis: *Steel. Res. Int.*, 2015, vol. 86, pp. 651–61.
62. H. Mio, M. Kadowaki, S. Matsuzaki, and K. Kunitomo: *Miner. Eng.*, 2012, vol. 33, pp. 27–33.
63. M. Ichida, K. Nishihara, K. Tamura, M. Sugata, and H. Ono: *ISIJ Int.*, 1991, vol. 31, pp. 505–14.
64. T. Fukushima, H. Nishio, Y. Ohno, T. Furukawa and T. Tzawa, *Symposium on Optimum Burden Distribution in the Blast Furnace*, 1978, pp. 7-1 - 7-14.
65. Y. Omori: *Blast Furnace Phenomena and Modelling*, 1st ed., Elsevier, New York, 1897, p. 631.
66. H. Takahashi, H. Kawai, M. Kobayashi, and T. Fukui: *ISIJ Int.*, 2005, vol. 45, pp. 1386–95.

Publisher's Note Springer Nature remains neutral with regard to jurisdictional claims in published maps and institutional affiliations.